High-Power Wireless Charging Of Heavy Duty EVs: Techniques, Challenges And Limitations

by John M. Miller and John Wolgemuth, Momentum Dynamics, Malvern, Penn.

Commercial high-power wireless charging equipment for light duty (LD) electric vehicles (EVs) has been available for several years. Suppliers now offer wireless EV supply equipment (WEVSE) in power ratings from 3.7 kW to 11.1 kW, and up to 22-kW developmental systems that are designed per SAE J2954.[1] The current LD standard "establishes an industry-wide specification guideline that defines acceptable criteria for interoperability, electromagnetic compatibility, minimum performance, safety and testing for wireless charging of light duty electric and plug-in electric vehicles." SAE J2954 will publish as a recommended practice level standard by year's end, meaning there is industry consensus on the testing procedures described therein.

Also in development since Feb. 2017 is a sister standard, SAE J2954/2 Wireless Power Transfer of Heavy Duty Plug-In Electric Vehicles and Positioning Communication, for which SAE points out "there are significant differences between Power Classes of Light Duty (3.7-22 kW) in SAE TIR J2954 and TIR J2954/2, Heavy Duty (HD) (up to 200 kW) vehicles for wireless charging." This article evaluates the practical and safety related limitations to high-power WPT, especially for heavy duty (HD) vehicles such as shuttle and transit bus, material handling, truck, rail, aerospace and marine.

Fig. 1 illustrates the case of WEVSE for HD vehicle charging at power levels of 25 kW to 60 kW and higher. Low-power WPT installations such as SAE J2954/1 cover coupler magnetic separation, or z-gaps of z1 (100 to 150 mm), z2 (140 to 210 mm) and z3 (170 to 250 mm SUV case)[1] for compact EVs like the Nissan LEAF and Chevy Bolt, which have nominal ground clearance of 160 mm. HD vehicles on the other hand will have z-gaps of 275 mm to >300 mm due to their larger ground clearance. The large magnetic gap makes transferring high kilowatt levels of power challenging[2], as will be discussed in this article.

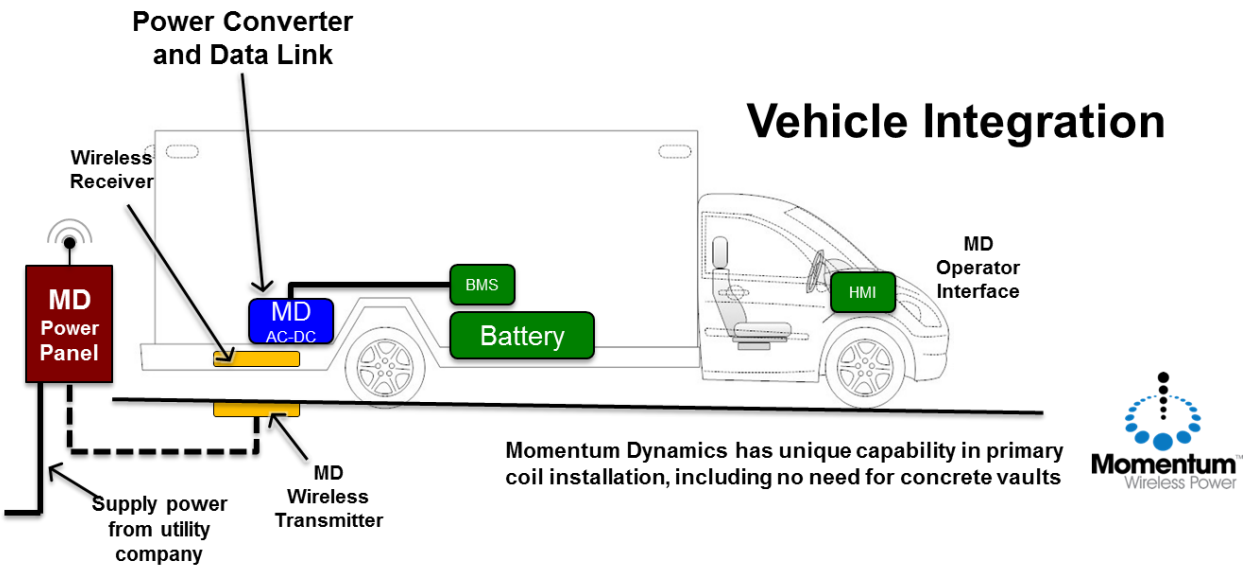

Fig. 1. Commercial high-power WPT with flush-mounted GA for HD vehicle (from reference [2])
Transmitter: ground assembly (GA) and Receiver: vehicle assembly (VA).

Understanding Wireless Power Transfer (WPT)

In reference [3] Andrew Daga points out that high-power WPT is now commercially available and the market poised for its acceptance because of the considerable benefits accrued from wireless charging. For example, convenience and robustness owing to hassle free charging and no worries about vandalism when the GA is embedded in concrete. The authors in references [4] and [5] highlight further practical attributes and implementation considerations for high-power WPT that benefit developers.

There is also considerable literature available on the theoretical aspects of WPT from two of its early pioneers[6], from others doing deep dives into power electronic requirements[7], and from researchers engaged in powering vehicles from the roadway[8] of which we'll have more to say in an upcoming section.

Fig. 2 illustrates the functional organization of a WPT installation when a vehicle is present for charging. As shown, there will be a cascade of at least of four power processing stages, perhaps five if the design includes an isolation/matching transformer. To meet the target efficiency of 85% grid to vehicle battery means each of the five stages must be 97% efficient. With modern wide bandgap semiconductors the power factor corrector (PFC), the high frequency (HF) inverter, and full-wave diode rectifier stages easily meet the requirement. This means that the coupler and compensation, or impedance matching networks (IMN) must also be of high quality and high efficiency.

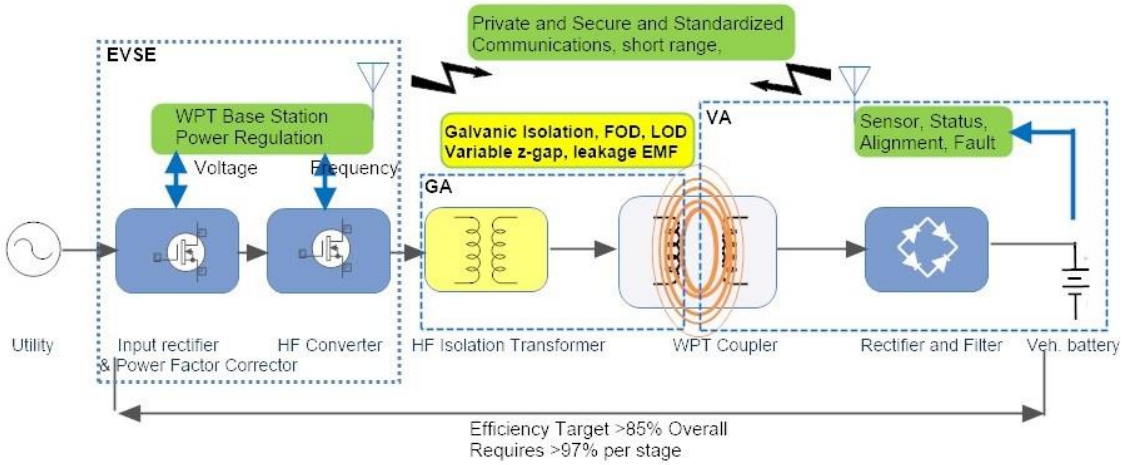

Fig. 2. Architectural elements of WPT installations (from reference [3]). FOD = foreign object detection, LOD = living object detection and EMF = electromagnetic field.

As Fig. 2 shows, the active front end, or PFC stage functions to meet grid power quality requirements on power factor (PF) and total harmonic distortion (THD) of >95% and <5% respectively. These are part of J2954, but also considered in SAE J2894, and in J3068 for three-phase EV charging (J3072 covers overhead charging and communications for HD vehicles).

Of special interest for high-power operation are dc fast charging (DCFC) equipment in which the cable and connectors are required to be liquid cooled for >80 A (3.6-mm pins) operation, and use larger, 6-mm pins if >120 A. Table 1 summarizes the standardized utility connections available for high-power EVSE operating off a three-phase grid supply. Table 2 illustrates representative power levels of the grid supply.

Table 1. Standardized three-phase grid-connection voltages.

U.S. 3-phase connections and configuration				Canada		Europe	
U_{ll}/U_{ph} (Vrms)	Config	U_{ll}/U_{ph} (Vrms)	Config	U_{ll}/U_{ph} (Vrms)	Config	U_{ll}/U_{ph} (Vrms)	Config
208/120	Y	480/277	Y	600/348	Y	400/230	Y

Table 2. Standardized three-phase grid-connection power levels.

Type	Voltage U_{ll}/U_{ph} (Vrms)	Config	Line Current (Arms)	Supply rating (kW)
AC	208/120	3-ph Y	80	30
AC	480/277	3-ph Y	11	13
AC	480/277	3-ph Y	80	65
AC	480/277	3-ph Y	160	133
DC	50V to 1000V	dc	1,000	20 to >500

WEVSE installations will require these same utility connections for high-power operation. For this reason, public installations such as big box stores, shopping centers, and workplace charging are the most likely dedicated charging sites to become available.

Referring to Fig. 2 the HF power inverter switching frequency (f_s) and duty cycle (d) along with PFC stage adjustable output voltage (U_{do}) are available inputs for power regulation and control. Although not clearly illustrated here the impedance matching networks (IMNs) and coupler are perhaps the main features of WPT that remain a mystery to some because of unfortunate labeling in the literature as "magnetic resonance".

Yes, the coupler and matching (or compensation) networks introduce a fourth-order state equation into the functionality along with several resonances. These can be clearly seen by examination of the energy storage components in Fig. 3: primary compensating capacitance, C_p; GA coupler leakage inductance, L_{lp}; secondary, or VA side of coupler leakage inductance, L_{ls}; and secondary compensating capacitance, C_s and resonances among them. In this figure the coupler consists of two planar, spiral wound, single-layer coils having ferrite spoke backing above an aluminum shield plate. More details on this appears in the following subsections.

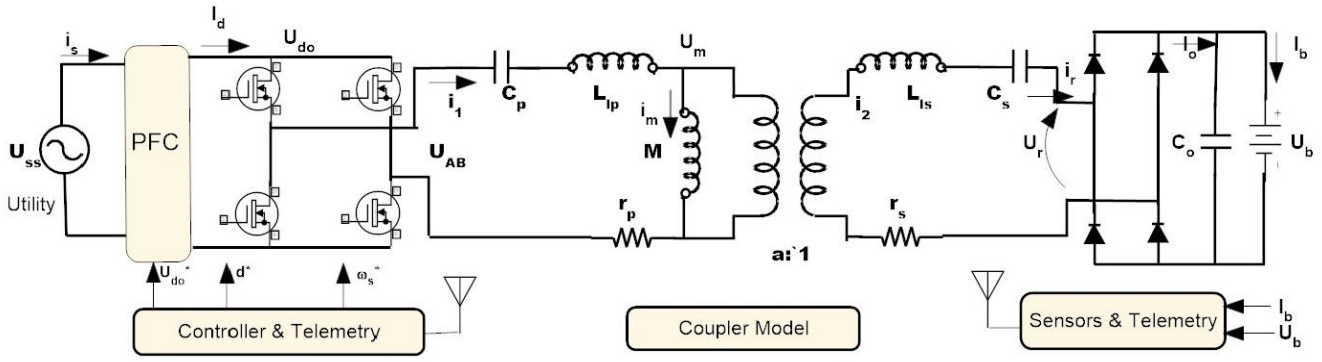

Fig. 3. Generalized WPT, series-series (S-S) compensated, with a non-unity turns ratio coupler.

The PFC stage applies adjustable dc voltage, U_{do}, to the HF inverter that has controllable duty cycle, d, at a variable frequency, f_s, so that its HF output voltage U_{AB} can be fully manipulated as in equation (1). The usual procedure in WPT is to use first harmonic analysis (FHA) so (1) is the fundamental only.

$$U_{AB1} = \frac{2\sqrt{2}}{\pi} U_{do} sin\left(\frac{d\pi}{2}\right) cos(\omega_s t) \qquad (Vrms) \tag{1}$$

In the series-series (S-S) compensated WPT all the coupler currents are sinusoidal but the driving point voltage, U_{AB}, and receiving point voltage, U_r, are square-wave (diode rectifier (DR) with capacitive output filter). The value of receiving end voltage, U_r, at the input of the full bridge DR, has its magnitude defined by the vehicle battery pack voltage, U_b.

$$|U_r| = \frac{2\sqrt{2}}{\pi}[U_b + 2U_{dio}] \qquad (Vrms) \tag{2}$$

It must be pointed out that at the full bridge DR the frequency of input current, i_r, is defined by the HF inverter. Consequently, and due in part to the switching point of the diodes, there will be some small lagging phase between the current, i_r, and voltage, U_r. In high-power WPT this can be accounted for by adding a small inductance (~1.3 μH) to the secondary-side leakage (or from computation of the DR reactive power component at its input). The DR input current, i_r, needed to support a given dc charging current, I_b, to the battery is given as equation (3).

$$|i_r| = \frac{\pi}{2\sqrt{2}} I_b = \frac{\pi}{2\sqrt{2}} \frac{P_o}{U_b} \qquad (Arms) \tag{3}$$

Since U_r and i_r are essentially in phase, the DR input power is the product of equations (2) and (3) and equates to battery charging power, $P_b = U_b I_b$ plus conduction and switching losses in the rectifier. Practical aspects of high-power WPT and interoperability are covered by the authors of references [9] and [10], while the authors of [11] also consider some electromagnetic topics related to the coupler design. The present work considers a more detailed look into the power limitations of WPT.

The key performance metrics to be evaluated in this article are:

- the reasonable limitations on coefficient of coupling (k) for this coupler when applied to a HD vehicle
- thermal constraints on the current density in the Litz cable given air cooling (convection only for stationary charging)
- safety considerations related to electromagnetic field intensity at the surface of the GA coil during high-power operation and
- practical limits set by insulation materials, in particular the Litz cable jacket and insulating layers in the ground assembly (GA), and vehicle assembly (VA) coupler pads.

Each of these limitations is evaluated in the following subsections where reference is made to Fig. 4, which highlights the key WPT component, the coupler. Note that the operating frequency is standardized at f_s = 85 kHz, a nominal point within the range of 81.38 kHz to 90.00 kHz, which is specified in J2894. This may change as J2954/2 evolves for HD vehicle charging.

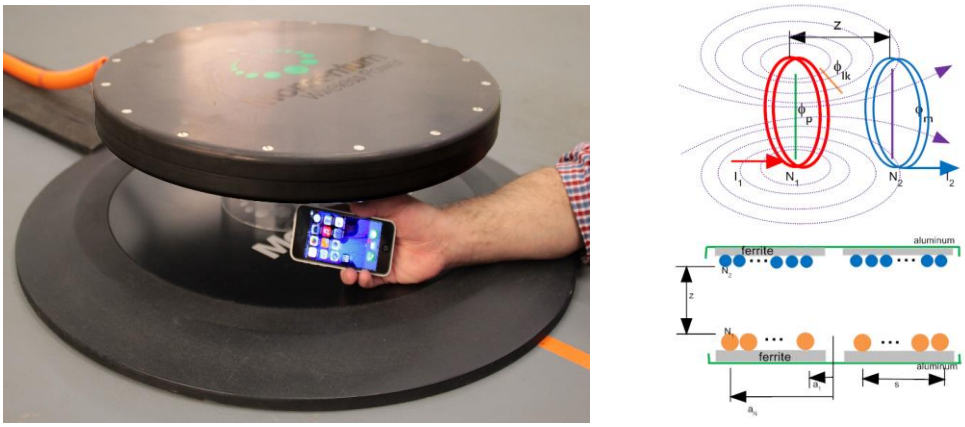

Fig. 4. High-power WPT coupler (photo at left, Courtesy of Momentum Dynamics) and material layout of GA and VA along with magnetic coupling definitions (diagram on right).

Coefficient Of Coupling

Fig. 4 illustrates the basic principles of coupler design, in this case a basic circular design which covers a somewhat rectangular to a square or polygon layout, and what's referred to as a "fountain field" of magnetic flux. At the right in Fig. 4 is a detail of how the coupler is constructed along with an illustration of its magnetic flux components.

Notice that the single-layer planar winding forms a band, or coil span (cs), of spiral wound Litz cable. In addition, the z-gap is technically defined as the distance between current in GA coil and current in the VA coil conductors as shown. Magnetically, only a fraction of GA (primary) coil flux, ϕ_p, links the VA (secondary) coil, ϕ_m, of this loosely coupled transformer. The remainder, and majority of flux, is leakage flux, ϕ_{lk}.

The ratio of mutual flux to primary flux is defined as coefficient of coupling, $k = \phi_m/\phi_p$, and it can be quite low. Electrically, and for good efficiency, the GA and VA coils should be high Q, that is have relatively low resistance compared to reactance. There is on-going debate[12] over the need for high k or high Q in WPT and some even prefer to use a figure of merit, kQ.

For high-power operation a high k has many benefits and in fact nominal values should be in the range $0.12 < k < 0.34$. In this article we use the geometric mean: k = 0.2 and design accordingly. The authors in reference [4] developed an empirical rule relating coil radius to z-gap that we incorporate here as equation (4) to find the mean, or effective coil radius, a, given inner and outer radii a_i and a_o respectively as shown in the detail of Fig. 4.

$$k \approx \frac{1}{\left\{1 + 2\left(\frac{z}{a}\right) + 2\left(\frac{z}{a}\right)^2\right\}^{\frac{3}{2}}} \tag{4}$$

Setting z = 0.3 m and k = 0.2 in (4) and solving the resulting quadratic for equivalent radius "a" yields: a = 0.5 m. In order to fully resolve the coil dimensions we require two additional geometric constraints.

$$a = \sqrt{a_i a_o}, and\ let\ cs = 0.65 a_o \tag{5}$$

The first constraint we noted above. The second follows from practical construction and magnetic efficiency noting that a small radius loop coupling to a larger radius loop makes only a small contribution to flux. The coil span may be manipulated, but a nominal of 65% of outer radius is considered reasonable. Solving equation (5) using the results of (4) yields (6).

$$a_o = \frac{a}{\sqrt{(1-0.65)}} = \frac{0.5}{\sqrt{0.35}} = 0.845m, \quad a_i = 0.35a_o = 0.295m, \text{ and } cs = 0.65a_o = 0.55m \tag{6}$$

With equation (6) the coil dimensions are specified for operation over the large z-gap required in HD vehicles. We also point out that the VA package space on a HD vehicle having rear axle with dual tires is 1.88 m of inside track, which does accommodate an outer diameter of $2a_o$ = 1.69 m.

Thermal Constraint

The next limitation that comes into play is keeping the coupler cool during high-power throughput. For this paper air cooling, or convection only, is assumed since charging is stationary. In reference [4] the authors point out that air cooling constrains current density in the Litz winding to $3 < J_{Litz} < 5$ A/mm^2 so that conductor temperature rise remains less than about 80˚C (the temperature limit specified in J2894). WPT designers may reduce this further depending on what foreign materials may be present on the GA surface in order to restrict object heating. More on that in the next subsection.

Fig. 5 provides a visualization of heat removal path from the coupler cables as described by the authors in reference [2]. Note that high thermal gradients are encountered across each electrical insulating layer such as wire coating, cable covering, and insulation material layers needed for electrical isolation. As such, thermal and isolation voltage constraints become coupled.

In the derivations to follow a conductor current density of J_{Litz} = 3.52 A_{rms}/mm^2 is used for convection.

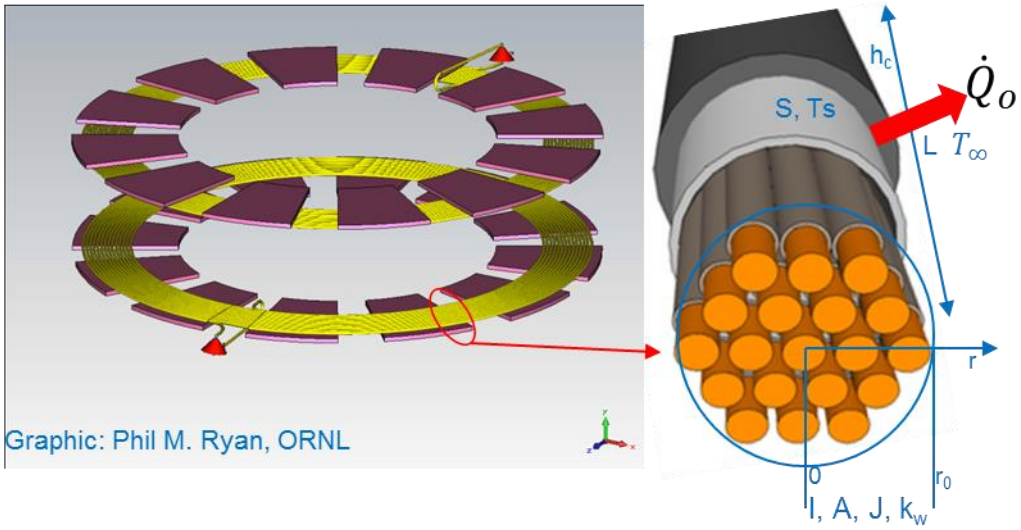

Fig. 5. Litz cable windings for high-power WPT (from reference [2]).

An assessment of the heat generation in the conductor volume for a given material type and placement requires use of Fourier's heat law and Newton's convection law in cylindrical coordinates and is beyond the scope of this article. However, interested readers may find the following metrics useful: cable internal heat conductivity k_w ~ 0.9 (W/mK) based on heat flow across coated conductors in a bundle having 63% fill factor; estimated free air convection coefficient, h_c ~ 5 W/m^{2}K from the winding to air, where temperature is in Kelvin (these metrics as

used in motor analysis are credited to Kevin Bennion and Gilbert Moreno of the DOE National Renewable Energy Laboratory, NREL in Golden, CO).

Fig. 6 considers the layout of Litz cables across the coil span assuming multiple conductors per winding turn (i.e., c-branches) as may be necessary to simultaneously meet thermal and total current limits, and to minimize winding thickness for package constraints.

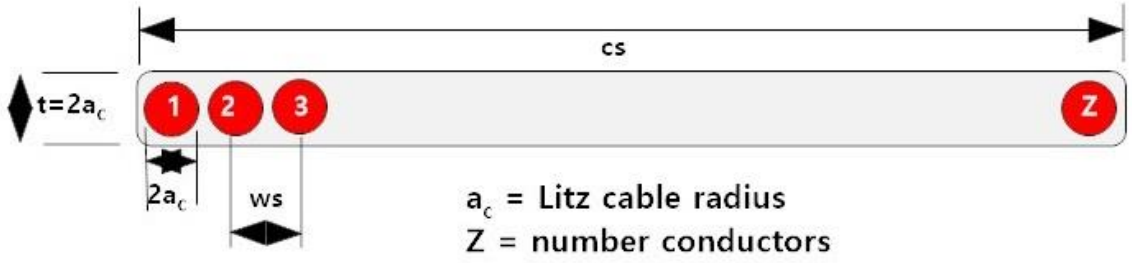

Fig. 6. Coupler winding design showing general case of total conductors, Z.

Total current that can be applied to the GA coil Litz cable is restricted to the current density limit noted above. For the general case of multiple conductors per winding turn the primary current is given as equation (7), where f_p is the Litz bundle packing factor (manufacturer dependent) and a_c the equivalent conductor radius.

$$i_1 = ci_{cond}, where\ \ i_{cond} = \pi f_p a_c^2 J_{Litz} \tag{7}$$

At this point the remaining two limits of surface field intensity and voltage stress of the winding come into play. In the next subsection, we address the limitation imposed by surface field intensity, H_y. Then, we consider the resulting computation of number of total turns, $N_1 = Z/c$. This parameter drives the coil inductance and this in turn, along with operating frequency, f_s, defines the voltage stress and insulation requirements.

Field Intensity At Surface Of Winding

In a practical design the electromagnetic field intensity just above the conductors shown in Fig. 6 requires detailed finite element analysis. For our purposes we consult the text by Clayton R. Paul[13] on the field and flux density of a finite width (infinite length) current sheet to approximate the coil span. The construct of Fig. 7 helps to illustrate the procedure where the sought after surface field intensity, H_y, is shown as being equal to the current sheet magnitude, K_x. This is an approximation, but suffice it to say that for flux guides having infinitely high permeability this would be the case.

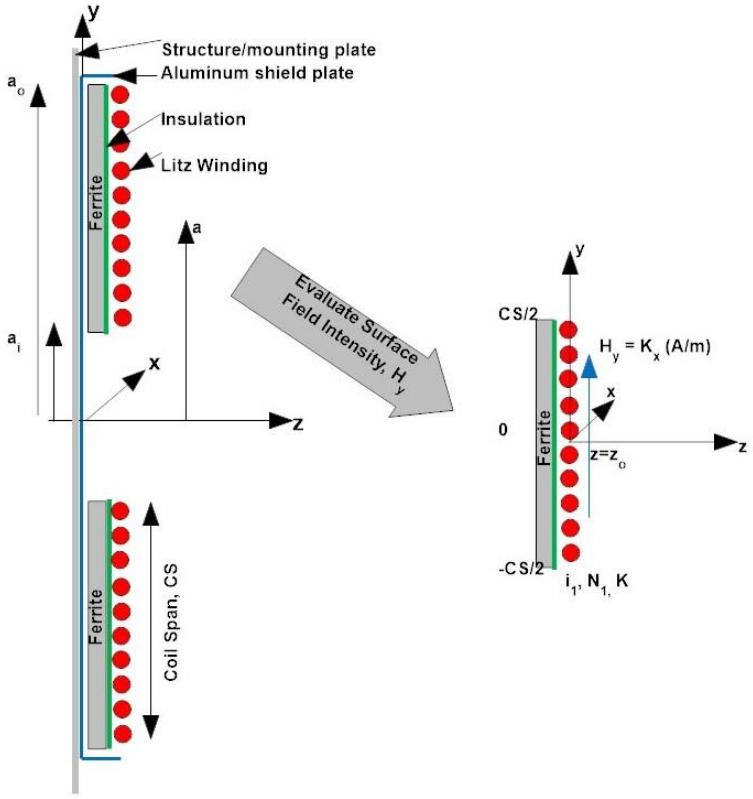

Fig. 7. Construct for approximating the surface field intensity of a WPT pad.

In practice the surface field measurement would use a laboratory three-axis field probe having 10-mm diameter. Considering that the GA has a non-magnetic cover of reasonable thickness the coil conductor to sensor probe will have z_o ~ 15 mm. From reference [13] the surface field intensity at z_o given infinite x-axis extent is given as equation (8).

$$H_y = \frac{K_x}{\pi}\tan^{-1}\left(\frac{cs}{2z_o}\right) \tag{8}$$

As cs→infinity (8) converges to $K_x/2$, which is the no ferrite case given in [13] meaning the result for ferrite guides may underestimate the H-field. In reality, ferrite spokes only provide partial coverage and are needed to meet VA package mass constraints so (8) is left as is.

A safety consideration regards the presence of combustible materials such as foil backed paper or clipped or stapled papers on the GA surface. For this article we take that limit as B_y < 3.5 mT. Using this limit and rearranging (8) results in the maximum allowable current sheet as equation (9).

$$K_x = \frac{\pi B_y}{\mu_o \tan^{-1}\left(\frac{cs}{2z_o}\right)} \rightarrow \frac{0.875x10^4}{\tan^{-1}\left(\frac{0.55}{0.03}\right)} = 5770\ A/m \tag{9}$$

Using (9) we can partially resolve the limit on number of turns, N_1, but not entirely.

$$N_1 i_1 = K_x cs = 5770(0.55) = 3173\ At \tag{10}$$

Referring to Fig. 6 one can see that the total number of conductors, Z, in the coil span, cs, is governed by the cable winding spacing, ws as defined in (11). Setting parameter ws > $2a_c$ is necessary to minimize proximity effects.

$$z = \frac{cs}{ws} \tag{11}$$

Before proceeding it is necessary to set a bound on the winding thickness, t, in Fig. 6 by setting some package constraints on the VA pad. Fixing an overall pad height of 40 mm (manufacturers may use maximum packaged mass instead, or both) and the following thicknesses: mounting plate (12 gauge steel 7/64 in.) of 2.78 mm, aluminum (6011) shield of 0.7 mm, as pressed ferrite flux guides (spokes) of 20 mm, Dupont Kapton insulating sheet of 0.15 mm, and cover plate of 3 mm. This leaves 40-2.78-0.7-20-0.15 = 16.36 mm = $2a_c$. New England Wire offers Litz cable of 50-kHz to 100-kHz frequency rating in #1AWG that has an overall diameter of 14 mm. With cable jacket and potting in the coil this just meets the packing space available.

For Litz cable one cannot simply apply equation (7) because of the extreme stranding. For a_c = 7 mm (#1 AWG Litz has area 84000 CMIL or 42.56 mm^2). Using this and the J_{Litz} constraint results in i_{cond} = 150 Arms.

Given the package coil height of 16.36 mm and taking the conductor winding spacing (11) as 3 a_c to minimize proximity effects results in a total number of conductors, Z = 24 (this value must be integer).

Insulation Material Voltage Limits

All the pieces so far are insufficient to define the complete winding because for large loops the inductance per turn will be high. High inductance and high operating frequency mean the reactive voltage stress will become extreme. Coil inductance is estimated using the Wheeler formula of a loop (refer to reference [13]).

$$L_p = \mu_o N_1^2 a \left\{ \ln\left(\frac{8a}{a_c}\right) - \frac{7}{4} \right\} \tag{12}$$

Our final limit is a practical and safety-related one that the voltage stress on the energy storage components is within a reasonable bound. For LD vehicles today and operating at 85 kHz the authors see reluctance to operate past 10-kV to 15-kV stress levels on coils and compensating capacitors. In the present article the limit will be set to 15 kVrms (21.2 kVpk) as an attainable maximum. This was partly the motivation for insulation materials in the coupler design, but became even more important for the series-compensating capacitors, C_p (and C_s), shown in Fig. 3 that will need to be series-parallel combinations of standard sizes.

The reader can easily see that the reactive burden on these components is going to be extreme. In fact, most developers would argue for <10 kVpk even at high power. In the interest of providing more insights into WPT the procedure continues at the higher limit defined by (13) for maximum stress.

$$U_{ms} = \omega_s L_p i_1 < 15kVrms \tag{13}$$

The limitations are now combined into a table to highlight maximum coil turns allowed (Table 3).

Table 3. Summary of WPT limitations when Z = 24.

Limit c (conductors/turn)	4	3	2	1
Number of turns, N_1	6	8	12	24
Field intensity, i_1 (Arms)	<529	<396	<264	<132
Inductance L_p (μH)	<103.9	<184.8	<415.8	<1663.2
Voltage stress U_{Lp} (kVrms)	<8.32	<14.8	<33.3	<133.2

Therefore, a coil of this large size should not exceed 8 turns even when using 3 conductors/turn. For this case the conductor current density is easily met (will be cooler) but the voltage stress remains high.

Tuning High-Power WPT

A high-power WPT having the S-S compensated architecture of Fig. 3 and parameter values of Table 3 are used to size the remaining parameters. In this example, and for both GA and VA of the same overall dimensions,[5] the same conductors may be used since both currents are approximately the same relative magnitude. Also, the GA and VA turns are taken as the same so no winding ratio is necessary (e.g., as shown for the ideal transformer of Fig. 3). The Litz cable cited has a resistance of 464 μΩ/m and an overall length for N_1 = 8t of 25.13 m. The coil resistances, $r_p = r_s$ =(25.13 x 464)/3 = 3.89 mΩ. The leakage and magnetizing inductances are defined as:

$$L_{lp} = L_{ls} = (1-k)L_p, \text{ and } M = k\sqrt{L_p L_s} \tag{14}$$

For operation at f_s = 85 kHz the nominal resonant angular frequency ω_o = 0.534 x 10^6 rad/sec. Here, the VA compensation is set to fully compensate the secondary leakage inductance as a starting point.

$$C_s = \frac{1}{\omega_o^2 L_{ls}} \rightarrow \frac{3.507x10^{-12}}{142.8x10^{-6}} = 23.72 \text{ nF} \tag{15}$$

The remaining parameters are tabulated in Table 4.

Table 4. Model parameters for high-power WPT.

Parameter	Value	Parameter	Value
GA inductance, L_p (μH)	184.8	Coefficient coupling, k (unitless)	0.2
Leakage inductance, L_{lp} (μH)	147.84	VA inductance, L_s (μH)	184.8
Mutual inductance, M (μH)	36.96	Leakage inductance, L_{ls} (μH)	147.84
GA coil resistance, r_p (mΩ)	3.89	VA coil resistance, r_s (mΩ)	3.89
Primary Capacitance, C_p (nF)	21.95	Secondary Capacitance, C_s (nF)	23.72
MOSFET Res, r_{mos} (mΩ)	0.8	Diode resistance, r_{dio} (mΩ)	0.5

Some researchers will tune the S-S compensation on the GA side so that C_p will resonate with the full primary inductance, L_p. Doing so will yield good, but not optimal, power throughput. In our tuning methodology the GA compensation capacitor is selected to resonate with the series path consisting of L_{lp}, L_{ls}, and C_s in order for full transmission across the power handling components. This again is a benefit of designing for higher values of k since the mutual branch inductance and reactance will be higher. This interim tuning capacitance is C_T defined in equation (16) showing that its resonance is shifted above ω_o according to the nominal coefficient of coupling.

$$C_T = \frac{C_p C_s}{(C_p + C_s)} = \frac{1}{(1+k^2)\omega_o^2 (L_{lp} + L_{ls})} = 11.4\ nF \tag{16}$$

Rearranging (16) yields the primary compensating capacitance, C_p, value as equation (17).

$$C_p = \frac{C_T C_s}{(C_s - C_T)} = \frac{289.8}{12.76} = 21.95\ nF \tag{17}$$

Lithium-ion battery packs in HD vehicles today, such as those used in transit buses, are in the range of 500 V. In the following simulation section the battery pack will be taken as lithium-nickel-manganese-cobalt Li(NMC)O_2 in a 138 S x 8 P x 40 Ah configuration with the WEVSE set to operate from a 480-Vac, three-phase, utility connection. At this supply voltage the nominal dc link voltage on the HF inverter will be approximately U_{do} = 2.34 x 277 = 648 Vdc and battery pack U_b = 138 x 3.6 = 497 Vdc. This represents a very reasonable matching level for tens of kilowatts of power.

Simulation Of The S-S Compensated WPT

Using the circuit model shown in Fig. 8, simulations are carried out using PSIM V.11.03 for the case of WEVSE connected to a 480-Vac, three-phase utility supply, full-wave rectified as the base case resulting in a dc link voltage of 648 Vdc according to equation (18).

$$U_{do} = \frac{3\sqrt{6}}{\pi} U_{ph} = 2.34(277) = 648 Vdc \tag{18}$$

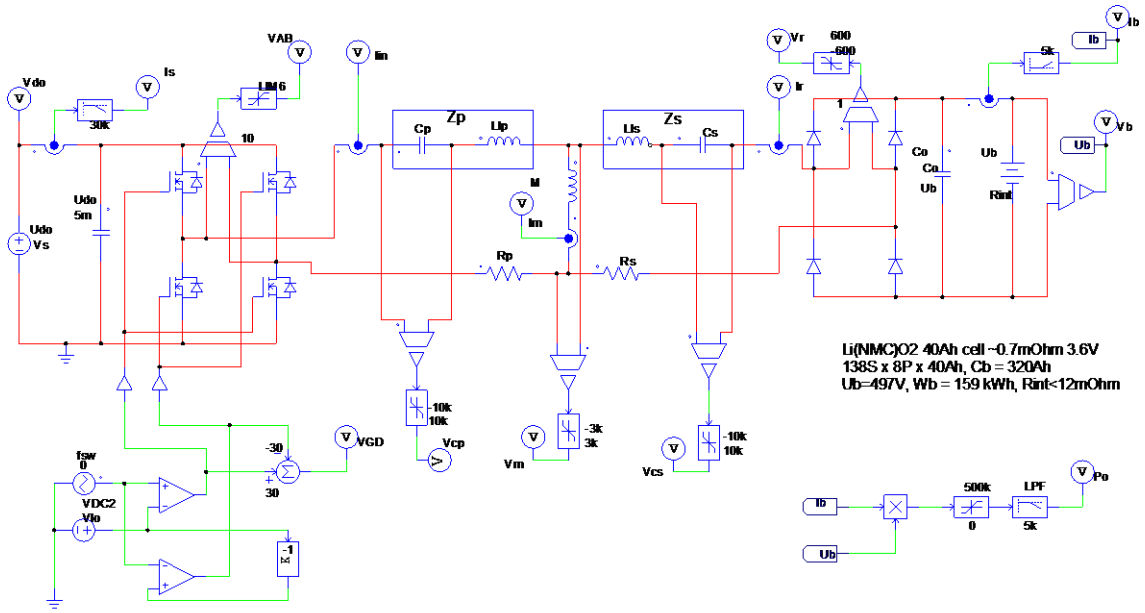

Fig. 8. HP S-S compensated WPT using the parameter values of Table 4 with a 138 S x 8 P x 40 Ah battery for 497 V, 320 Ah, 159 kWh, and R_{int} = 12 mΩ.

The battery pack under charge has sufficient energy for a transit bus. In this case the rectifier input voltage U_r, (2) and current i_r, (3) are computed as:

$$U_r = \frac{2\sqrt{2}}{\pi}[U_b + 2U_{dio} + I_b R_{int}] \quad (Vrms), \quad i_r = \frac{\pi}{2\sqrt{2}} I_b \quad (Arms) \tag{19}$$

The coupler has the same GA and VA turns number as in Table 3 so the ideal level-translation transformer of Fig. 2 is omitted from the equivalent "T" model. Computed values are given by (14) and used in the model.

Simulation Model

The compensated leakage inductances shown as impedances, Z_p, and Z_s, the main contributors to reactive power provided by compensating capacitors to the S-S WPT along with shedding more insight into its power throughput versus frequency behavior. This is also why re-tuning is necessary to optimize the throughput power for given value of k.

$$\omega_p^2 = \frac{1}{L_{lp}C_p}, \ \omega_p = 0.5549x10^6, \quad Z_p = \frac{j}{\omega_s C_p}\left[\left(\frac{\omega_s}{\omega_p}\right)^2 - 1\right] = \frac{jG_p}{\omega_s C_p} \tag{20}$$

$$\omega_{os}^2 = \frac{1}{L_{ls}C_s}, \ \omega_{os} = 0.5338x10^6, \quad Z_s = \frac{j}{\omega_s C_s}\left[\left(\frac{\omega_s}{\omega_p}\right)^2 - 1\right] = \frac{jG_s}{\omega_s C_s} \tag{21}$$

Table 5. Retuning of C_s based on simulation results (fs = 85 kHz, ω_s = 0.534 x 10^6 and C_p = 21.95 nF.)

C_s (nF)	26.3	26.5	26.6	27
P_o (kW)	56	57.5	87.3	57.9

As the results in Table 5 show, there can be some rapid transitions in impedances for slight variations in the VA side compensating capacitance. This will become clear in the following section when the Thevenin equivalent impedance of the S-S compensated WPT is discussed. In Table 5 the frequency and primary capacitance are fixed.

Fig. 9 illustrates the output power given U_{do} = 648 Vdc, U_b = 497 Vdc, and f_s = 85 kHz but with C_s = 26.6 nF according to Table 5.

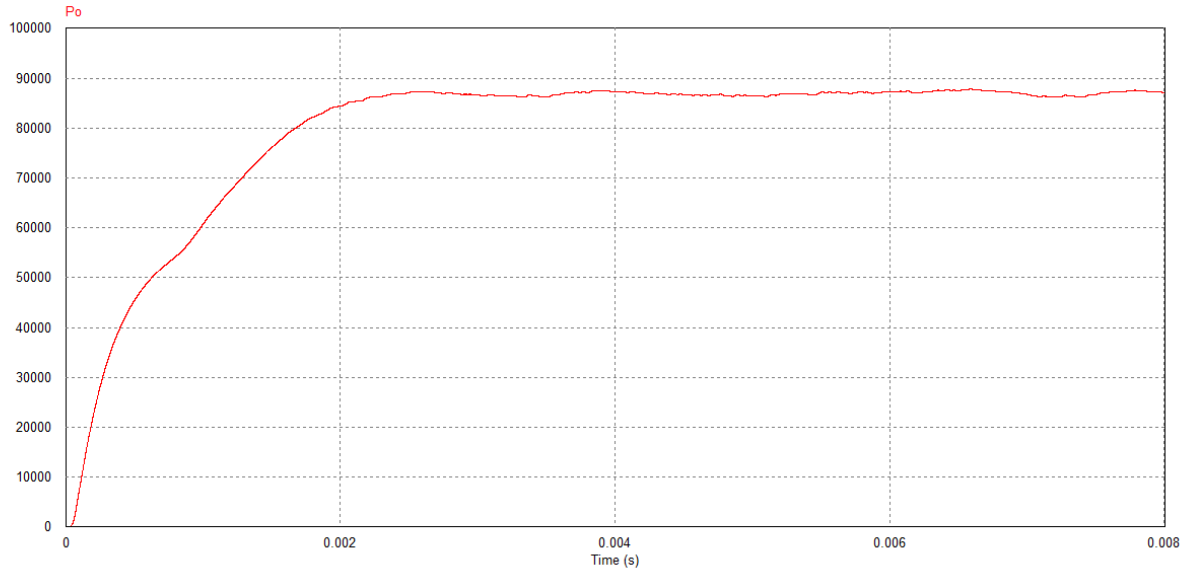

Fig. 9. Simulated power output given a 480-Vac three-phase utility supply and with the output tuned for P_o = 87.3 kW. Currents: i_{in} = 281.5 Arms, i_r = 192.68 Arms and i_m = 91.93 Arms; Voltages: U_{AB} = 647 V, U_r = 500 V, U_m = 1.81 kVrms and I_b = 174.6 Adc.

Voltage stress on the compensating capacitors is extremely high as expected: U_{Cp} = 23.94 kVrms, U_{Cs} = 13.55 kVrms. Developers know that compensating capacitors for high-power WPT require very high VAR rating. In this case C_p must handle 281.5 Arms at 23.94 kVrms for 6739 kVAR. Also, the two-step character shown in Fig. 9 at start-up is not clear because for the C_s values either side of 26.6 nF this does not occur.

Comparing these results with those shown in Table 3 shows that some margin exists before the limits are reached. So, the simulation was repeated with a higher value of dc link voltage. At U_{do} = 900 V the power output rises to 143 kW into the 497-V battery pack but the limits of Table 3 for the coupler and compensation network are now exceeded. In this case i_{in} = 489.6 Arms, i_r=336.5 Arms and U_{Cp} = 41.8 kVrms.

Results And Key Waveforms

The waveforms of most interest in WPT are the HF inverter output voltage and current supplied to the IMN and coupler and the DR input voltage and current. These are shown in Fig. 10 with heavy traces for the GA side and lighter traces for the VA side. Of particular interest is that both U_{AB} and U_r are in phase, i_r is essentially in phase with U_r but i_{in} lags U_{AB} by a few degrees. Resonant voltages for the respective currents are either leading or lagging current by 90˚.

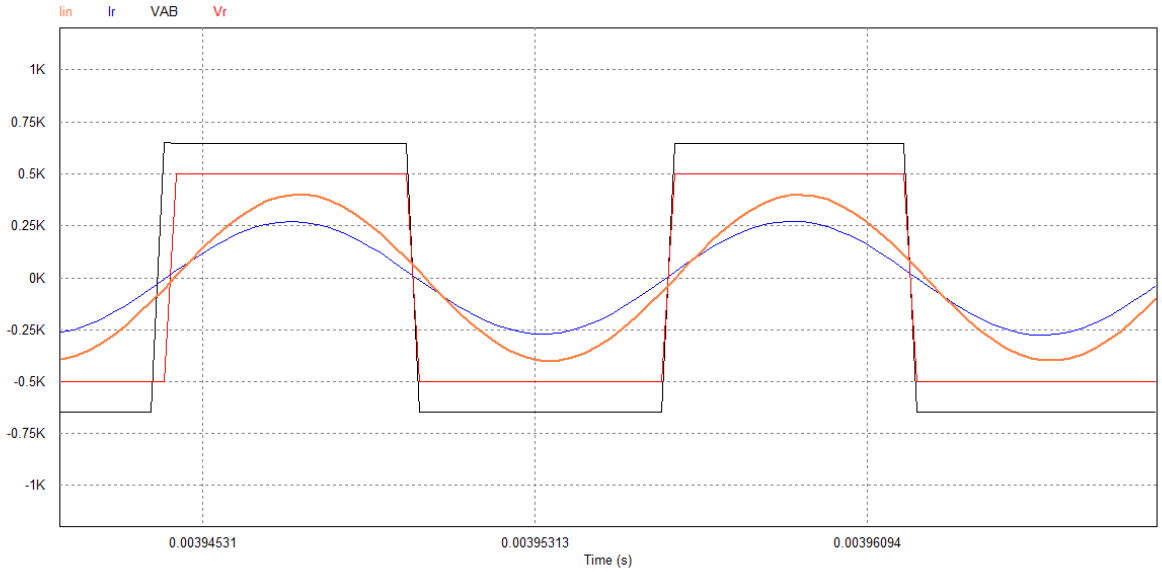

Fig. 10. HF inverter waveforms UAB and i_{in}, DR waveforms U_r (black) and i_r (red) currents: i_{in} = 281.5 Arms (orange), and i_r = 192.8 Arms (blue).

A final point on the simulation is that one may apply Kirchhoff's voltage law around the GA and VA loops that intersect on the coupler magnetizing branch, M. For the GA loop the voltages are $U_{AB} = U_{Zp} + U_m$ with all variables as phasors. For example, $|U_{Zp}|$ = 1.734 kVrms and $|U_m|$ = 1.84 kVrms with angles given by those shown in Fig. 10 and the "j" operator of equations (20) and (21). For the VA loop the voltages are $U_m = U_{Zs} + U_r$, again benefiting from a phasor construct and noting that $|U_{Zs}|$ = 1.767 kVrms. Interested readers may wish to construct phasor diagrams keeping phasor $\vec{U}_m$ common to both loops to show that the resultants are U_{AB} and U_r. Voltage harmonics of U_{AB} and U_r are beyond the scope of this article.

A Thevenin equivalent may be constructed by reference to Fig. 11 using equations (20) and (21), plus the following definitions in equations (22) and (23) that describe two additional resonances; ω_{mp} for C_p and M and ω_{ms} for C_s and M.

$$\omega_{mp}^2 = \frac{1}{MC_p};\ \ G_{mp} = \left(\frac{\omega_s}{\omega_{mp}}\right)^2 \tag{22}$$

$$\omega_{ms}^2 = \frac{1}{MC_s};\ \ G_{ms} = \left(\frac{\omega_s}{\omega_{ms}}\right)^2 \tag{23}$$

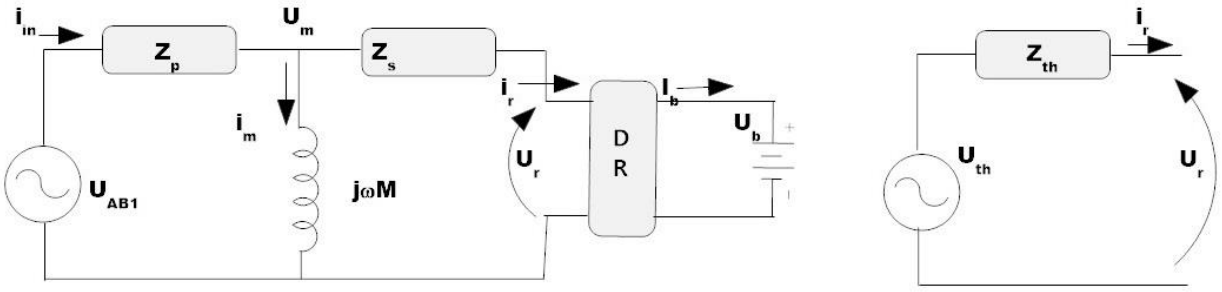

Fig. 11. S-S compensated WPT model and Thevenin equivalent.

Referring to Fig. 11 and equations (20) through (23) the Thevenin impedance and voltage are given as equations (24) and (25) where the impedance is found by shorting voltage sources and combining parallel branches.

$$Z_{th} = \frac{j\left[G_s\left(G_p + G_{mp}\right) + G_p G_{ms}\right]}{\omega_s C_s\left(G_p + G_{mp}\right)} \tag{24}$$

$$U_{th} = \frac{G_{mp} U_s}{\left(G_p + G_{mp}\right)} \tag{25}$$

For the same parameter values used to obtain the result shown in Fig. 9 to develop the expression in (24) and by applying an equivalent load resistance R_{eq} = 4.45 Ω, then equation (25) results in the output power versus frequency result shown in Fig. 12. In fact, at f_s = 85 kHz the Thevenin model predicts i_r = 192.4 Arms in relatively good agreement with PSIM for this power output.

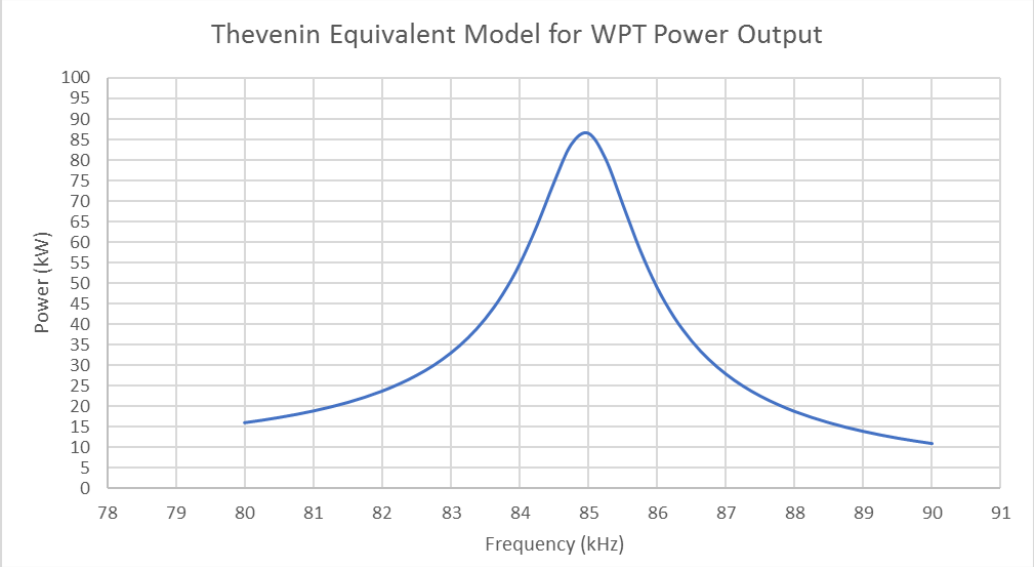

Fig. 12. Thevenin model predicted $P_r(f_s) = P_o(f_s)+P_{DR}(f_s)$ using equations (24) to (26) $|i_r|$ = 192.4 Arms and P_r = 96.2 kW into the DR.

The WPT throughput power, $P_r(f_s)$, is computed by referring to Fig. 11 when the Thevenin model is terminated with an equivalent load resistance R_e = 4 Ω as equation (26). In this idealized case (r_p = r_s = 0) the Thevenin impedance Z_{th} is purely imaginary. Readers are informed that the Thevenin impedance function, $Z_{th}(f_s)$, crosses through zero at frequency f_s.

$$P_r = \frac{U_{th}^2}{\sqrt{R_e^2 + Z_{th}^2}} \quad (W) \tag{26}$$

Insight into the point about C_s sensitivity in the section on the simulation model can be found in equations (24) and (25) which show that only Z_{th} contains parameter C_s and then only in the denominator function (26) for throughput power.

Comments On Leakage Fields

A further topic that always comes up in discussions on WPT regards fringe, or leakage fields. These EMFs are a safety concern as pointed out by Dr. Schrafel[14], especially with people having implanted medical devices (IMDs). The authors[15] performed experimental evaluation of the leakage EMF of a high-power WPT for HD vehicle charging and found these to be within acceptable levels, but the transit bus experimented on had a kneeling feature that closed the z-gap substantially.

For larger gaps necessary in HD vehicle charging the concern is relevant and the reason that Momentum Dynamics engaged Dr. Patrick Reilly[16] for assistance on the physiological effects of EMFs on humans. Dr. Reilly also made substantial contributions to the industry standard on EMF led by the IEEE and issued as C95.2345 (NATO)[17] in which general population exposure levels for EMF below 100 kW (nerve stimulation effects) are substantially higher than the guidelines in use from ICNIRP-2010[18] at 27 μTrms and adopted in SAE J2954/1.

For LD vehicles the leakage EMF at the vehicle external perimeter and within the passenger cabin are further limited to 15 μTrms by the U.S. FDA and the American Association Medical Instrumentation (AAMI) (Fig. 13). The physiological effect of frequencies > 100 kHz is primarily tissue heating.

Fig. 13 Illustration of leakage EMF (graphic courtesy Oak Ridge National Laboratory) and coupler field pattern (graphic courtesy of the University of Texas-Dallas (UTD) and [11]).

WPT chargers must also meet FCC part 18 radiated emission limits at 10 m of <100 dBμA/m (in Japan this same H-field limit at 10 m is 68.4 dBμA/m). Test and validation of these levels requires open-field testing with appropriate ground plane. Considerable model, simulation, and experimental work will be involved in the development of a standard for HP WPT (SAE J2954/2) due to the large z-gaps involved and the necessity of meeting fringe-field EMF limits.

Momentum Dynamics High-Power WPT

High-power WEVSE has been under development and commercialization at Momentum Dynamics since 2009 for shuttle and bus applications. Fig. 14 shows one such application using a large-footprint GA pad and WPT charging over a 300-mm z-gap. Early systems operated at 20 kHz because of the limitations discussed above in the section "Understanding Wireless Power Transfer (WPT)".

At this writing SAE J2954/2 is under development and many of the limitations discussed will need to be resolved before interoperable and coexistence standards can be firmed up. As one would expect, the prominent interoperable feature will be the ability of an LD vehicle to charge over an HD GA pad and vice-versa. If the interoperable frequency remains at 85 kHz then significant obstacles will arise as noted earlier for high power.

Whereas if an LD/HD feature of the WEVSE is to include a 4:1 frequency selection that charges LD at f_s = 85 kHz and HD at 21.25 kHz then some limits are mitigated at the expense of 4x higher magnetizing current in the GA pad at the lower frequency. This again is why a high coefficient of coupling, k, is so vital in HD charging.

Fig. 14. A high-power WEVSE GA for HD vehicle charging (courtesy of Momentum Dynamics).

Another, and perhaps more commercially viable option, is to cluster smaller WEVSE GA pads, so that power transfer of hundreds of kilowatts becomes feasible. As interest grows in the area known as "Xtreme" charging (150 kW to 400 kW) there are commercial conductive charging systems that require multiple cable/connector arrangements, liquid-cooled cable/connectors, and battery voltage increases from 350 V to 800 V to accommodate such power levels. With S-S compensated WPT we have already seen that unboosted operation off 480-Vac, three-phase above 60 kW becomes problematic with a 350-V battery but doable for a 500-V pack.

Fig. 15 illustrates a Momentum Dynamics high-power building block GA pad suitable for clustering in groups of two, four, or more. For example, a cluster of four such pads rated at 50 kW each suffices for transit bus WPT charging at 200 kW.

Fig. 15. Clustering high-power WPT (50-kW GA pad shown).

In this "divide and conquer" approach, the pads will need to be properly phased. For example, they may be configured in pairs of reference phase and anti-phase in order to implement a "donut" field pattern between GA and VA pairs.

Future Prospects

There is considerable and growing interest in using high-power WPT for in-motion charging[19] as the ultimate solution to EV range anxiety. But as have seen in this article, high-power throughput places high stress on reactive components, which in turn demands use of dielectric and insulation materials capable of low loss and durable construction along with novel packaging design. There are effectively two scenarios for in-motion charging, also called dynamic WPT charging DWPT: first, is to have a long sequence of roadway embedded GA pads, and second, a continuous cable.

In the first instance, rectangular-shaped pads are energized sequentially with the passing vehicle to develop a traveling wave of charging power beneath the vehicle and synchronized with it. This requires extremely fast communications such as NFC—near field communications developed and in use at Momentum Dynamics[20] that has <5-μs latency, and most importantly is node to node, private and secure link-up. Sequenced GA pads may be energized either from a voltage source inverter (VSI) and high-voltage dc distribution, or from a single current source inverter (CSI) and cable that supplies each of the GA pad drivers.

The second scenario relies on a CSI-driven cable that is embedded, but near the top, of the roadway along with specialized VA pick-up pads as discussed by the author and contributors in reference [21]. A typical implementation of such continuous cable GAs will use regulated 200-Arms formed by a VSI HF inverter and LCL impedance matching network tuned as a gyrator[22]. In these systems a fixed source voltage, U_{AB1}, forces a fixed cable current, i_{in}, to use our existing terminology. The effect of additional loading, such as the presence of a second vehicle, is to force the load side voltage higher, which then translates through the impedance inverting gyrator into higher input current on the GA side.

In addition to the manner in which the roadway GA is implemented, there are additional concerns related to lateral offset of VA from the GA, GA response time, pulsation power reflected to grid supply, and in case of cable systems—persistent EMFs. The first of these is solved when the vehicle (could be an autonomous vehicle) has lane-following capability and the second by NFC with advanced turn-on control. The third point is more problematic as utility operators are not as concerned with the high power as with intermittency. This point was addressed by the authors in reference [23] by using local energy storage on the GA side to smooth supply pulsations as GA units are sequenced with the passing vehicle.

Summary

The analysis provided in this article highlights some of the challenges facing WPT operation above 100 kW, the region that SAE J1772 conductive charging and suppliers refer to as Xtreme charging (150 kW to 400 kW). There are a several factors that play a major role at these power levels, necessitating a divide and conquer approach in WPT. One factor is that 85-kHz operation results in extreme voltage stress on reactive components. Another is that the attendant high k implies large diameter coils, which again forces excessive voltage stress.

In addition to voltage stress on components there are concerns such as surface field intensity on the GA pad when foreign objects may be present (for example, foil backed paper), plus leakage electromagnetic fields, EMF, in proximity to the vehicle. Meeting regulatory requirements for human exposure levels plus those for radiated emissions at 10 m (and 30 m) is also problematic for high-power WPT when large z-gaps are involved.

In general, with large z-gaps, individual WPT couplers will be limited to roughly 50 kW to 90 kW each. This is because, at large diameters, the high inductance means very high resonant voltages and expensive compensation capacitors.

The conclusion for high-power WPT is that clustering coupler pads alleviates many concerns and limitations of a single large pad by summing multiple sources, each of which meets a set of constraints. This is akin to the main

mirror of the Hubble space telescope, which achieves the effect of one large mirror while being composed of many smaller mirror segments.

References

1. "Wireless Power Transfer for Light-Duty Plug-In Electric Vehicles and Alignment Methodology," available as J2954-201605 SAE Technical Information Report.

2. "Wireless Power Transfer: A Developers Guide" by John M. Miller, Andrew Daga, Bruce R. Long, and Peter C. Schrafel, IEEE APEC2017 Industry Session, Tampa Convention Center, Tampa, FL, 26-30 March 2017.

3. "Electric Fuel Pumps for Wireless Power Transfer—Enabling the Rapid Growth in the Electric Vehicle Market," by Andrew Daga, John M. Miller, Bruce R. Long, Peter Schrafel and John Wolgemuth, IEEE Power Electronics Magazine, June 2017, pp. 2-12.

4. "Elements of Wireless Power Transfer Essential to High Power Charging of Heavy Duty Vehicles, " by John M. Miller and Andrew Daga, IEEE Transactions on Transportation Electrification, Vol. 1, No. 1, June 2015.

5. "What All Technology Adopters Should Know About WPT For High Power Charging," Tutorial Presentation, IEEE PELS Workshop on Emerging Technologies: Wireless Power, WOW2016, Holiday Inn Hotel, Knoxville, TN, 4-6 October 2016

6. "Modern Trends in Inductive Power Transfer for Transportation Applications" by Grant A. Covic and John T. Boys, IEEE Journal of Emerging and Selected Topics in Power Electronics, Vol. 1, No. 1, March 2013.

7. "Inductive Power Transfer for Electric Vehicle Charging: Technical Challenges and Trade-offs" by Roman Bosshard and Johann W. Kolar, IEEE Power Electronics Magazine, Vol.3 No.3, pgs. 22-30, September 2016.

8. "Advances in Wireless Power Transfer Systems for Roadway-Powered Electric Vehicles" by Su Y. Choi, Beom W. Gu, Seog Y. Jeong and Chun T. Rim, IEEE Journal of Emerging and Selected Topics in Power Electronics, Vol. 3, No. 1, March 2015

9. "Practical and Implementation Issues of Wireless Power Charging of EV's" by John M. Miller, IEEE Transportation Electrification eNewsletter on WPT, Third Quarter 2014.

10. "Interoperable solution for wireless EV charging – challenges" by Grzegorz Omback, IEEE VTC Workshop on Wireless, WOW2014, Conrad Seoul Hotel, 18 May 2014, Korea.

11. "Optimization of a Contactless Power Transfer System for Electric Vehicles" by Saeed Hasanzadeh, Sadegh Vaez-Zadeh and Arash Hassanpour Isfahani, IEEE Transactions on Vehicular Technology, Vol. 61, No.8, pp. 3566-3573, 2012.

12. "The WPT Dilemma – High K or High Q?" by John M. Miller, Peter C. Schrafel, Bruce R. Long and Andrew Daga, IEEE Workshop on Wireless, WOW2016, Hilton Hotel, Knoxville, TN, 4-6 October 2016.

13. "Inductance – Loop and Partial" by Clayton R. Paul and J. Wiley & Sons, pp.62-67, copyright 2010.

14. "The Reality of Safety Concerns Relative to WPT Systems for Automotive Applications" by Peter C. Schrafel, Bruce. R. Long, John M. Miller and Andrew Daga, IEEE Workshop on Wireless, WOW2016, Hilton Hotel, Knoxville, TN, 4-6 October 2016.

15. "Very-Low-Frequency and Low-Frequency Electric and Magnetic Fields Associated with Electric Shuttle Bus Wireless Charging," by R.A. Tell, R. Kavetz, J.R. Bailey and J. Halliwell, Radiation Protection Dosimetry, pp. 1-12, published by Oxford University Press, 15 September 2013.

16. "Human Exposure Standards in the Frequency Range 1 Hz to 100 kHz: The Case for Adoption of the IEEE Standard" by J. Patrick Reilly, Health Physics Society, Vol. 107, No. 4, Oct. 2014 (www.health-physics.com).

17. IEEE Std C95.1-2345-2014, "IEEE Standard for Military Workplaces—Force Health Protection Regarding Personnel Exposure to Electric, Magnetic, and Electromagnetic Fields, 0 Hz to 300 GHz," 16 May 2014

18. ICNIRP 2010, "Guidelines for Limiting Exposure to Time-varying Electric, Magnetic, and Electromagnetic Fields (UP TO 300 GHz)," published in Health Physics 99(6):818-836; 2010.

19. "ORNL Experience and Challenges facing Dynamic Wireless Power Charging of EV's" by John M. Miller, P.T. Jones, Jan-Mou Li, and Omer C. Onar, IEEE Circuits and Systems Magazine, pp. 40-52, Second Quarter 2015.

20. "A Near Field Communications System for Wireless Power" by Bruce R. Long, IEEE Workshop on Wireless, WOW2016, Hilton Hotel, Knoxville, TN, 4-6 October 2016.

21. "The Development of Shaped Magnetic Fields in Resonance for EV's and Trains KAIST" by Chun T. Rim, IEEE VTC Workshop on Emerging Technologies: Wireless Power (2014 IEEE VTC-WoW), Conrad Seoul hotel, Seoul, Korea, 18 May 2014.

22. "Trends in Wireless Power Transfer and its Commercialization" by John M. Miller, Invited IEEE PEL's Presentation to Dallas section, University of Dallas-Texas (UTD) ECEN, 22 September 2017

23. "Demonstrating Wireless Charging of an Electric Vehicle" by John M. Miller, Omer C. Onar, Cliff White, Steven Campbell, Chester Coomer, Larry Seiber, Raymond Sepe Jr., and Anton Steyerl, IEEE Power Electronics Magazine, pp. 12-24, March 2014.

About The Authors

John M. Miller is owner and founder of J-N-J Miller Design Services PLLC, which was established in 2002 to provide professional consulting for industry. Miller has over 41 years of experience in electrical engineering across various industries that include automotive, aerospace, white goods, and electrical practice. He joined Momentum Dynamics Technical Advisory Board in 2014 as senior scientist working on wireless power transfer for heavy-duty vehicles.

His previous work experience includes Distinguished R&D Scientist at Oak Ridge National Laboratory (ORNL) where he held positions as director of the Power Electronics and Electric Power Systems Research Center, and served as program manager of the DOE Vehicular Technologies subprogram APEEM. Previously, Miller held various engineering and senior management positions at Maxwell Technologies, Ford Motor Company, and Texas Instruments.

He has published several books related to wireless charging, ultracapacitor applications (translated to Chinese in 2015), propulsion systems for hybrid vehicles (translated to Chinese 2016), automotive power electronics, and vehicular electric power systems. He holds a B.S.E.E. from the University of Arkansas-Fayetteville, M.S.E.E. from Southern Methodist University, Dallas, TX, and Ph.D. from Michigan State University, East Lansing, MI. Miller is a Life Fellow of the IEEE, Fellow of the SAE, and a registered professional engineer in Michigan (1980) and in Texas (2014). He can be reached at jmmiller35@aol.com.

John Wolgemuth is the principal power electronics engineer at Momentum Dynamics, a developer of wireless charging and power electronics technologies for the automotive industry. He is responsible for power electronics design for new systems entering the commercial and automotive markets.

Before joining Momentum Dynamics, Wolgemuth was the lead engineer for a contractor that provided V2G PEV equipment to the Department of Defense. This equipment was deployed across three domestic military bases in aggregate excess of 500 kW. Each installed system was integrated with on-base energy management systems and vehicle reservation platforms to provide support to the local utility while maintaining reliable availability of the EVs. Wolgemuth also worked on deployments of stationary energy systems as second life applications for OEM EV battery packs.

Wolgemuth holds a B.S.E. in both electrical engineering and mechanical engineering from Messiah College, Mechanicsburg, Penn. He is a member of IEEE, a member of SAE, and a registered professional engineer in Pennsylvania (2017). He can be reached at John.Wolgemuth@MomentumDynamics.com.

For more information on wireless charging, see the How2Power Design Guide, locate the Popular Topics category and select "Wireless Power".